Nonequilibrium phonon tuning and mapping in few-layer graphene with infrared nanoscopy

Jun Qian, ^{1,2,3} Yilong Luan, ^{1,2} Minsung Kim, ^{1,2} Kai-Ming Ho, ^{1,2} Yi Shi, ³ Cai-Zhuang Wang, ^{1,2,*}, Yun Li, ^{3,*} and Zhe Fei^{1,2,*}

J.Q. and Y.L. contributed equally to this work.

*Corresponding authors.

(C.Z.W) wangcz@iastate.edu, (Y.L.) yli@nju.edu.cn, (Z.F.) zfei@iastate.edu.

Abstract

Electron-phonon interactions are fundamentally important physical processes responsible for many key discoveries in condensed matter physics and material sciences. Herein, by exploiting the scattering-type scanning near-field optical microscope (s-SNOM) excited with a femtosecond infrared (IR) laser, we explored the strong coupling between IR phonons in few-layer graphene (FLG) with ultra-hot electrons, which are heated up by the intense laser field enhanced by the s-SNOM tip. More specifically, we found that the intensity of the phonon resonance can be tuned systematically by varying the laser power that controls the electron temperature. Furthermore, the high spatial resolution of s-SNOM allows us to map the local phonon characteristics at sharp boundaries and nanostructures. Our findings offer insights into the intriguing physics behind the electron-phonon interactions in nonequilibrium conditions and open new pathways for manipulating phonons with optical means.

Main text

In recent years, graphene and its thicker counterparts attract tremendous research interest owing to their superior properties [1-3], which profoundly promote both fundamental sciences and technological applications [4-7]. Nearly all the electronic, optical, and thermal properties of these materials are closely related to the responses of electrons, phonons, and their coherent interactions. Indeed, electron-phonon interactions are responsible for many peculiar physical phenomena in graphene and few-layer graphene (FLG), such as Fermi-velocity renormalization [8,9], giant tunneling conductance [10], magnetophonon oscillations [11,12], and unconventional superconductivity [13,14]. These fascinating phenomena have therefore inspired further studies of graphene phonons and their coupling with electronic excitations in the 2D flatland.

Infrared (IR) spectroscopy has been proven to be a powerful tool in probing optical phonons in FLG (i.e. two layers and above) [15-18], but not in single-layer graphene (SLG) due to the lack of net dipole moments. There are many unique phenomena related to IR phonons in FLG, among which the "charged-

¹Department of Physics and Astronomy, Iowa State University, Ames, Iowa 50011, United States.

²Ames Laboratory, U. S. Department of Energy, Iowa State University, Ames, Iowa 50011, United States.

³National Laboratory of Solid-State Microstructures, School of Electronic Science and Engineering, Collaborative Innovation Center of Advanced Microstructures, Nanjing University, Nanjing 210093, People's Republic of China.

phonon" effect attracts a lot of research interest [15-22]. This effect is originated from the coupling between IR phonons with interband electronic excitations in FLG, resulting in interesting gate-tunable phonon anomalies. So far, the studies of IR phonons of FLG and their interactions with electrons were performed mainly by far-field spectroscopy that typically has a low excitation power due to the usage of weak IR sources (e.g. Globar). Therefore, IR phonons are coupled with relatively cold electrons at equilibrium conditions. Responses of graphene phonons interacting with nonequilibrium hot electrons remain largely unexplored.

In this Letter, we report a nano-IR spectroscopy study of phonon responses in FLG using the scattering-type scanning near-field optical microscope (s-SNOM) that is built on an atomic force microscope (AFM) (see Supplemental Material [23]). By coupling s-SNOM with a broadband femtosecond (fs) laser, we were able to perform IR spectroscopy with a high spatial resolution (~ 20 nm), which is convenient for probing and mapping small graphene microcrystals and nanostructures. The spectral window of the laser is selected to be 1100-1900 cm⁻¹ (corresponding to 0.14-0.24 eV) that covers the graphene phonon resonance (~ 0.2 eV). The fs laser has a pulse width of ~ 100 fs and average power up to 1 mW. With further enhancement by the conductive s-SNOM tip, electrons can be heated up to very high temperatures [23,24] and strongly impact the phonon resonance of FLG.

Our nano-IR setup is illustrated in Fig. 1(a), where the laser pulses are focused at the apex of the s-SNOM tip. The tip-scattered pulses, which are partially collected by the detector, contain key nano-IR signals of the sample right underneath the tip. By implementing a Michelson interferometer setup (Fig. S1), we can extract both the amplitude and phase of the nano-IR signals. We discuss in the main text the amplitude (s) signal that ideal for revealing phonon resonances [25,26]. The phase data are consistent with the amplitude and are discussed in the Supplemental Material [23]. Our samples were fabricated by mechanical exfoliations of bulk graphite onto the standard SiO₂/Si substrates. The thicknesses and stacking orders of graphene samples were determined by a combination of optical microscopy, AFM, and s-SNOM imaging (Fig. S2). Throughout the paper, we label the thickness of single-layer to penta-layer graphene as "1L" to "5L", respectively. For stacking orders, we use "AB", "ABA", etc. for Bernal stacking and "ABC", "ABCA", etc. for rhombohedral stacking.

In Fig. 1(b), we plot the nano-IR amplitude spectra $s(\omega)$ of graphene/graphite samples with various thicknesses and stacking orders. Here graphene samples were electrically doped by gating. All IR spectra were normalized to that of gold and displaced vertically for clarity. Gold is a standard reference material in IR due to the overall flat response. As shown in Fig. 1(b), there is one dominant resonance at ~1130 cm⁻¹ (blue arrow) in the spectra, which is attributed to the optical phonon of SiO₂ [25,26]. Besides, there is a weaker resonance feature centered at ~1580 cm⁻¹ (red arrow) in nearly all samples except SLG, ABA-3L graphene, and graphite, which is originated from the IR-active E_u or E' phonons [Fig. 1(c)] [15,22,27]. The IR phonon does exist in ABA-3L graphene and graphite, according to far-field studies [18,22], but they are too weak to be resolved by s-SNOM. Clearly, both the intensity and shape of phonon resonances are different from sample to sample. As reported previously [15,17,18], the observed thickness- and stacking-dependence of phonon resonances of FLG are directly linked to the coherent electron-phonon interactions. In this work, we focus on ABC-3L graphene for quantitative analysis of the hot-electron responses. Other FLG samples share similar responses and are discussed in the Supplemental Material [23].

We first performed nano-IR spectroscopy of FLG by tuning its carrier density with back gating. As an example, we plot in Fig. 2(a) gate-tunable IR spectra $s(\omega)$ of ABC-3L graphene. Here we label the difference between the gate voltage (V_g) and the charge-neutral voltage (V_{CN}), namely $V_g - V_{CN}$, which is proportional to the carrier density. We mainly focus on the hole doping side ($V_g - V_{CN} < 0$) in the current work. The responses of phonon resonances on the electron doping side are expected to be similar according to previous studies [15,18]. In all gating measurements, we used a low laser power ($\sim 78 \mu W$) that has relatively small heating on electrons. Clearly from Fig. 2(a), the phonon resonance demonstrates a systematic dependence with doping, which is a direct evidence of electron-phonon coupling. Gate-tunable IR phonons were also observed in other types of FLG (Fig. S3). Detailed discussions about gate-tunable phonons of FLG could be found in previous far-field studies [15,16,18].

While gating tunes the carrier density, varying the laser power (P) can effectively control the electron temperature (T_e) of graphene [24,28-30]. In Fig. 2(b), we plot the P-dependent nano-IR spectra of hole-doped ABC-3L graphene (V_g - V_{CN} = -80 V), where one can see that the phonon resonance shrinks systematically with increasing P. Following Ref. 15, we fit the background-subtracted phonon resonances

with the Fano formula $\Delta s(\omega) = (W/\Gamma)\{(q^2 + 2qz - 1)/[q^2(1+z^2)]\}$ with $z = 2(\omega - \omega_0)/\Gamma$. Here W

describes the phonon intensity, ω_0 is the resonance frequency, Γ is the linewidth, and q is the dimensionless parameter that describes Fano asymmetry. We discuss mainly the responses of W here, and the effects of other parameters are less prominent and are introduced in the Supplemental Material [23]. The extracted W of ABC-3L graphene is plotted in Fig. 2(c,d), where one can see that W can be controlled effectively by tuning V_g or P. More interestingly, the power dependence of W appears to be exponential while the gate dependence is approximately linear. Power-dependence measurements have also been performed in other FLG samples (Fig. S4). In all cases, exponential decay of the phonon intensity with increasing P has been observed.

Before discussing the power-dependent responses, we first briefly describe electron-phonon interactions for cold electrons at equilibrium conditions. According to previous studies [15-21], the interactions are mainly due to the coupling between the phonon resonance and interband transitions. More specifically, the strong interband resonance can transfer oscillator strength to the phonon resonance, thus significantly enhancing the latter. The interband transitions are also responsible for other interesting responses (e.g. Fano asymmetry and phonon softening) of the phonon resonance (see Ref. 15 and Supplemental Material [23]). Among all possible interband transitions, the most relevant ones to the phonon intensity are between the high-(low-) lying valence (conduction) bands in the case of hole (electron) doping. We sketched in Fig. 3(a) these interband transitions (blue arrows) on the band structure of hole-doping ABC-3L graphene. The relatively flat bands close to the maxima of the valence bands [marked with E_H and E_L] result in high densities of states (DOS) [Fig. 3(b)] and hence strong interband transitions. From Fig. 3(a), one can see that more states are available for interband transitions at higher doping levels, which accounts for the observed gate dependence of phonon resonances in Fig. 2(a) [15,18]. For FLG with different thicknesses and stacking orders, the energy and intensity of the interband resonance vary from one to another [31], resulting in their unique phonon resonances and responses [see Fig. 1(b) and Refs. 15,17,18]. The hump-shaped interband resonance of the ABCAB-5L graphene with a linewidth of ~500 cm⁻¹ and a peak frequency of ~1800 cm⁻¹ (black arrow) can be seen in our nano-IR spectra (Fig. S3 and Fig. S4). In

the case of other FLG samples, the peak energies of the interband resonance are higher [31] and out of the experimental range [see Fig. 3(b) and Fig. S11].

When exciting graphene with tip-enhanced fs pulses, electrons can be heated up significantly. The heating is initiated by the absorption of broadband IR photons through both interband and intraband transitions. After an extremely fast carrier thermalization (< 30 fs) [24,29,30], carriers are characterized by a single Fermi-Dirac distribution with an effective T_e . To estimate T_e , we performed finite-element simulations considering tip-enhanced pulse heating, thermal transport, and electron-phonon heat transfer. Detailed discussions about the simulations are given in the Supplemental Material [23]. According to the simulations, the average T_e of ABC-3L graphene underneath the tip scales monotonically with laser power, and it can reach up to 1600 K at full laser power [Fig. S12(d)]. Electrons do transfer heat to optical phonons close to K and Γ points [Fig. S12(b)], but the entire lattice remains relatively cold, so the system is in a nonequilibrium state within the pulse duration [28].

The most obvious effect of hot electrons is the thermal broadening of the Fermi surface, which strongly affects the interband transitions responsible for phonon enhancement. To demonstrate that, we plot in Fig. 3(c) the electron occupation at both room temperature ($T_e = 300 \text{ K}$) and a high temperature ($T_e = 1600 \text{ K}$) based on the Fermi-Dirac function $f(E) = \{\exp[(E-E_F)/kT_e] + 1\}^{-1}$, where k is the Boltzmann's constant. We mark in Fig. 3(c) the relevant low (E_L) and high (E_H) energies for the key interband transitions sketched in Fig. 3(a). The Fermi energy (E_F) is estimated to be about -0.08 eV for ABC-3L graphene with $V_g - V_{CN} = -80 \text{ V}$ (hole doping), so E_F is sandwiched by E_L and E_H . At $E_R = 300 \text{ K}$, electron states are almost fully occupied at E_L and unoccupied at E_R , so interband transitions from E_L to E_H are largely unaffected. At $E_R = 1600 \text{ K}$, states at both E_L and E_H are partially occupied, so interband transitions will be suppressed.

For quantitative discussions, we refer to the charged-phonon theory of FLG introduced previously [20,21]. According to the theory, the phonon intensity W of FLG is proportional to $[\text{Re}(\chi)]^2$, where χ is the mixed current-phonon response function and can be obtained by summating $[f(E_i) - f(E_f)]/[\hbar\omega_0 - (E_f - E_i) + i\eta]$ over all the states for the relevant interband transitions. Here E_i and E_f are the energies for the initial and final states of transition, $\hbar\omega_0 \approx 0.2$ eV is the phonon energy, and η is the broadening parameter of interband transitions [21]. We set η to be 0.01 eV following a previous far-field study of ABC-3L graphene [32]. If considering only the key interband transitions sketched in Fig. 3(a) for approximation, W has the following relationship:

$$W(T_e) \approx A \left\{ \text{Re} \left[\frac{f(E_L) - f(E_H)}{\hbar \omega_0 - (E_H - E_L) + i\eta} \right] \right\}^2, \tag{1}$$

where A is a T_e -independent coefficient. Based on Eq. 1, we plot in Fig. 3(d) the normalized $W(T_e)$ curve of ABC-3L, where one can see that W drops systematically as T_e increases. The decay is exponential due to the factor $f(E_L)$ - $f(E_H)$, which accounts for the thermal broadening picture described above [Fig. 3(c)]. In Fig. 3(d), we also add the experimental data points of ABC-3L graphene after converting laser power into T_e based on the calculated P- T_e dependence curve [Fig. S13(d)]. The general trend of the theory curve matches that of the experimental data points. For more accurate calculations, one needs to consider all possible interband transitions and the temperature dependence of η .

Finally, we took advantage of the high-resolution capability of the s-SNOM to probe the nano-IR phonon characteristics of FLG. In Fig. 4, we present the results taken at two representative sample regions:

an ABC/ABA/ABC-3L graphene junction and an ABC-3L graphene nanobubble. The nanobubble here is formed when air, water, or hydrocarbons are trapped underneath the sample during the sample fabrication process [33-35]. In Fig. 4(a,b), we plot the s-SNOM and AFM images to reveal the local structure and geometry of the two sample regions. The nano-IR signal shown in the s-SNOM image [Fig. 4(a)] is integrated over the spectral range from 1100 to 1900 cm⁻¹. Figures 4(c) and 4(d) are hyperspectral maps with horizontal and vertical axes corresponding to the tip location (x) and IR frequency x, respectively. Each hyperspectral map consists of 40 nano-IR spectra taken as tip scans step by step (step size = 25 nm) along the white dashed lines in Fig. 4(a,b). We plot two representative spectra from each sample in Fig. 4(e,f), which correspond to the vertical line-cuts at marked locations (arrows) in the hyperspectral maps [Fig. 4(c,d)].

The dominant feature in the hyperspectral images [Fig. 4(c,d)] is the bright IR phonon line close to $\omega = 1580~\text{cm}^{-1}$ in ABC-3L graphene (marked with dashed lines). The phonon line is not seen inside ABA-3L graphene due to the extremely weak intensity as discovered earlier [17,18]. The sharp cut-off of the phonon line at the ABC-ABA boundary proves the high resolution (~25 nm) of our technique, which is required to probe small nanostructures. The ABC-3L graphene bubble shown in Fig. 4(b) is one such nanostructure. The diameter of the bubble is ~200 nm with a height of ~33 nm. Interestingly, we found that the phonon line curved downward in the bubble region. At the bubble center, the phonon frequency is ~1565 cm⁻¹, 16 cm⁻¹ lower than that of the flat sample region (~1581 cm⁻¹) [Fig. 4(f)]. The phonon softening is mainly due to the increase of tensile strain in the bubble region, which has been reported in previous Raman spectroscopy studies [36,37]. Nevertheless, the spatial resolution of far-field Raman spectroscopy is typically above 300 nm, which is not enough to resolve local strain distributions in small nanobubbles. In addition to phonon frequency, phonon intensity also drops significantly (by ~30% at the bubble center), which is partly due to the shift of the phonon frequency away from the interband resonance and partly due to the decrease of doping when the sample is away from the substrate [38]. The change of doping (< 5.8 × 10^{12} cm⁻²) also contribute slightly to the phonon softening, but it is estimated to be within 2 cm⁻¹ [18].

In summary, we have performed a comprehensive nano-IR spectroscopy study of the intrinsic phonons in FLG using s-SNOM excited with a broadband fs laser. We demonstrated that our nano-IR spectroscopy with a nanoscale resolution is convenient for probing and mapping the local phonon characteristics in FLG microcrystals and nanostructures. Moreover, we found that the IR phonon intensity decreases systematically with increasing laser power, which is attributed to the strong coupling between phonons and nonequilibrium hot electrons excited by the laser. Quantitative analyses and simulations indicate that the average T_e of electrons, which is tunable by controlling the power, can reach up to 1600 K and can thus significantly quench the interband transitions and hence the phonon resonance. Our work deepens the understanding of nonequilibrium electron-phonon interactions in FLG and paves the way for future studies in a wide variety of quantum systems (e.g. unconventional superconductors [39,40], Weyl semimetals [41], perovskite semiconductors [42], semiconductor quantum dots [43], etc.), where electron-phonon coupling plays an essential role. Unlike electrical gating that is only effective in 2D materials, tuning T_e with power control can be applied in materials of all dimensions.

Acknowledgments

Work done at Ames Laboratory was supported by the U.S. Department of Energy, Office of Basic Energy Science, Division of Materials Sciences and Engineering. Ames Laboratory is operated for the U.S. Department of Energy by Iowa State University under Contract No. DE-AC02-07CH11358. The sample preparation was supported by the National Science Foundation under Grant No. DMR-1945560. J.Q. is thankful to the China Scholarship Council (CSC) for financial support. Y.L. acknowledges the funding support from the Natural Science Foundation of Jiangsu No. BK20170075, and the National Natural Science Foundation of China Awards No. 61774080 and No. 61574074.

J.Q. and Y.L. contributed equally to this work.

*Corresponding authors.

(C.Z.W) wangcz@iastate.edu, (Y.L.) yli@nju.edu.cn, (Z.F.) zfei@iastate.edu.

References

- [1] A. H. Castro Neto, F. Guinea, N. M. R. Peres, K. S. Novoselov, and A. K. Geim, Rev. Mod. Phys. 81, 109-162 (2009).
- [2] S. Das Sarma, S. Adam, E. H. Hwang, and E. Rossi, Rev. Mod. Phys. 83, 407-470 (2011).
- [3] D. N. Basov, M. M. Fogler, A. Lanzara, F. Wang, and Y. Zhang, Rev. Mod. Phys. 86, 959-994 (2014).
- [4] F. Bonaccorso, Z. Sun, T. Hasan, and A. C. Ferrari, Nat. Photon. 4, 611-622 (2010).
- [5] F. Bonaccorso, L. Colombo, G. Yu, M. Stoller, V. Tozzini, A. C. Ferrari, R. S. Ruoff, and V. Pellegrini, Science **347**, 1246501 (2015).
- [6] T. Low and P. Avouris, ACS Nano 8, 1086-1101 (2014).
- [7] W. Han, R. K. Kawakami, M. Gmitra, and J. Fabian, Nat. Nanotechnol. 9, 794-807 (2014).
- [8] W.-K. Tse and S. Das Sarma, Phys. Rev. Lett. 99, 236802 (2007).
- [9] C.-H. Park, F. Giustino, M. L. Cohen, and S. G. Louie, Nano Lett. 8, 4229-4233 (2008).
- [10] Y. Zhang, V. W. Brar, F. Wang, C. Girit, Y. Yayon, M. Panlasigui, A. Zettl, and M. F. Crommie, Nat. Phys. 4, 627-630 (2008).
- [11] P. Kumaravadivel, M. T. Greenaway, D. Perello, A. Berdyugin, J. Birkbeck, J. Wengraf, S. Liu, J. H. Edgar, A. K. Geim, L. Eaves *et al.*, Nat. Commun. **10**, 3334 (2019).
- [12] C. Cong, J. Jung, B. Cao, C. Qiu, X. Shen, A. Ferreira, S. Adam, and T. Yu, Phys. Rev. B **91**, 235403 (2015).
- [13] Y. Cao, V. Fatemi, S. Fang, K. Watanabe, T. Taniguchi, E. Kaxiras, and P. Jarillo-Herrero, Nature **556**, 43-50 (2018).
- [14] B. Lian, Z. Wang, and B. Andrei Bernevig, Phys. Rev. Lett. 122, 257002 (2019).
- [15] A. B. Kuzmenko, L. Benfatto, E. Cappelluti, I. Crassee, D. van der Marel, P. Blake, K. S. Novoselov, and A. K. Geim, Phys. Rev. Lett. **103**, 116804 (2009).
- [16] T.-T. Tang, Y. Zhang, C.-H. Park, B. Geng, C. Girit, Z. Hao, M. C. Martin, A. Zettl, M. F. Crommie, S. G. Louie, Y. R. Shen, and F. Wang, Nat. Nanotechnol. 5, 32-36 (2010).
- [17] Z. Li, C. H. Lui, E. Cappelluti, L. Benfatto, K. F. Mak, G. L. Carr, J. Shan, and T. F. Heinz, Phys. Rev. Lett. 108, 156801 (2012).
- [18] C. H. Lui, E. Cappelluti, Z. Li, and T. F. Heinz, Phys. Rev. Lett. 110, 185504 (2013).

- [19] T. Ando, J. Phys. Soc. Jap. 76, 104711 (2007).
- [20] E. Cappelluti, L. Benfatto, and A. B. Kuzmenko, Phys. Rev. B 82, 041402 (2010).
- [21] E. Cappelluti, L. Benfatto, M. Manzardo, A. B. Kuzmenko, Phys. Rev. B 86, 115439 (2012).
- [22] M. Manzardo, E. Cappelluti, E. van Heumen, and A. B. Kuzmenko, Phys. Rev. B 86, 054302 (2012).
- [23] Supplemental Material for additional experimental & theoretical details and results.
- [24] M. Wagner, Z. Fei, A.S. McLeod, A.S. Rodin, W. Bao, E. G. Iwinski, Z. Zhao, M. Goldflam, M. Liu, G. Dominguez, *et al.*, Nano Lett. **14**, 894-900 (2014).
- [25] Z. Fei, G. O. Andreev, W. Bao, L. M. Zhang, A. S. McLeod, C. Wang, M. K. Stewart, Z. Zhao, G. Dominguez, M. Thiemens *et al.*, Nano Lett. **11**, 4701-4705 (2011).
- [26] L. M. Zhang, G. O. Andreev, Z. Fei, A. S. McLeod, G. Dominguez, M. Thiemens, A. H. Castro-Neto, D. N. Basov, and M. M. Fogler, Phys. Rev. B 85, 075419 (2012).
- [27] J.-A. Yan, W. Y. Ruan, and M. Y. Chou, Phys. Rev. B 77, 125401 (2008).
- [28] C. H. Lui, K. F. Mak, J. Shan, and T. F. Heinz, Phys. Rev. Lett. 105, 127404 (2010).
- [29] D. Brida, A. Tomadin, C. Manzoni, Y. J. Kim, A. Lombardo, S. Milana, R. R. Nair, K. S. Novoselov, A. C. Ferrari, G. Cerullo *et al.*, Nat. Commun. **4**, 1987 (2013).
- [30] Q. Ma, T. I. Andersen, N. L. Nair, N. M. Gabor, M. Massicotte, C. H. Lui, A. F. Young, W. Fang, K. Watanabe, T. Taniguchi *et al.*, Nat. Phys. **12**, 455-459 (2016).
- [31] D.S. Ki, H. Kwon, A. Y. Nikitin, S. Ahn, L. Martin-Moreno, F. J. Garcia-Vidal, S. Ryu, H. Min, and Z. H. Kim, ACS Nano 9, 6765-6773 (2015).
- [32] C. H. Lui, Z. Li, K. F. Mak, E. Cappelluti, and T. F. Heinz, Nat. Phys. 7, 944-947 (2011).
- [33] S. J. Haigh, A. Gholinia, R. Jalil, S. Romani, L. Britnell, D. C. Elias, K. S. Novoselov, L. A. Ponomarenko, A. K. Geim, and R. Gorbachev, Nat. Mater. 11, 764–767 (2012).
- [34] E. Khestanova, F. Guinea, L. Fumagalli, A. K. Geim, I. V. Grigorieva, Nat. Commun. 7, 12587 (2016).
- [35] Z. Fei, J. J. Foley, W. Gannett, K. K. Liu, S. Dai, G. X. Ni, A. Zettl, M. M. Fogler, G. P. Wiederrecht, S. K. Gray, and D. N. Basov, Nano Lett. 16, 7842-7848 (2016).
- [36] J. Zabel, R. R. Nair, A. Ott, T. Georgiou, A. K. Geim, A. S. Novoselov, and C. Casiraghi, Nano Lett. 12, 617-621 (2012).
- [37] D. Metten, F. Federspiel, M. Romeo, S. Berciaud, Phys. Rev. Applied 2, 054008 (2014).
- [38] S. Ryu, L. Liu, S. Berciaud, Y.-J. Yu, H. Liu, P. Kim, G. W. Flynn, and L. E. Brus, Nano Lett. 10, 4944-4951 (2010).
- [39] W. Weber, Phys. Rev. Lett. **58**, 1371 (1987).
- [40] T. Timusk, C. D. Porter, and D. B. Tanner, Phys. Rev. Lett. 66, 663-666 (1991).
- [41] B. Xu, Y. M. Dai, L. X. Zhao, L.X. Zhao, K. Wang, R. Yang, W. Zhang, J.Y. Liu, H. Xiao, G.F. Chen, S.A. Trugman, J.-X. Zhu, A.J. Taylor, D.A. Yarotski, R.P. Prasankumar, and X.G. Qiu, Nat. Commun. 8, 14933 (2017).
- [42] X. Gong, O. Voznyy, A. Jain, W. Liu, R. Sabatini, Z. Piontkowski, G. Walters, G. Bappi, S. Nokhrin, O. Bushuyev et al., Nat. Materials 17, 550-556 (2018).
- [43] S. Hameau, Y. Guldner, O. Verzelen, R. Ferreira, and G. Bastard, J. Zeman, A. Lemaître, and J. M. Gérard, Phys. Rev. Lett. 83, 4152-4155 (1999).

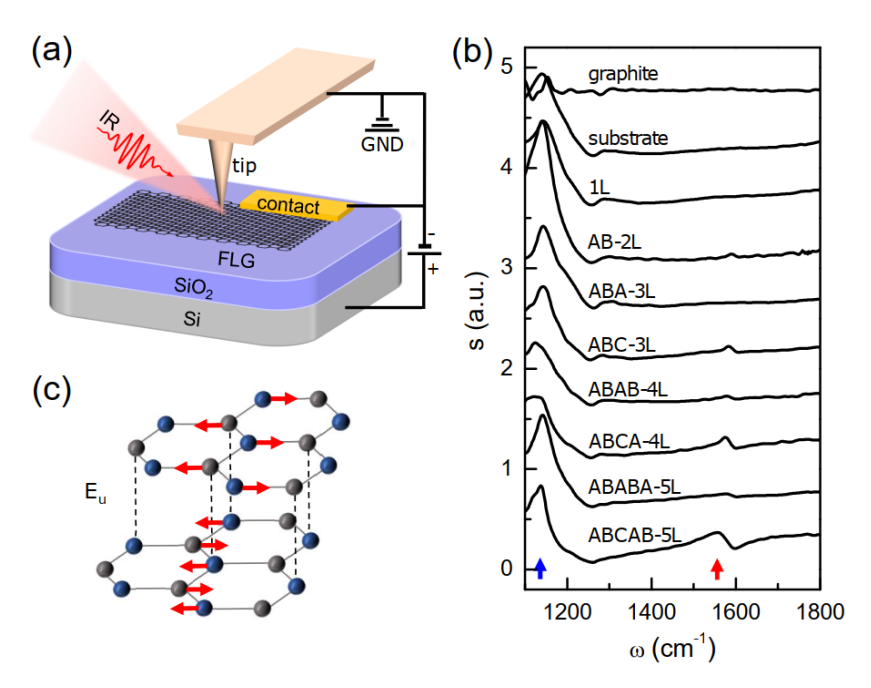


FIG. 1. (a) Illustration of the s-SNOM study of FLG excited by an fs IR beam. (b) The nano-IR spectra of the SiO_2/Si substrate, graphite, and graphene layer(s) with different thicknesses and stacking orders. Here we use 1L", "2L", ... to label the thickness, and use "AB", "ABA", "ABC", etc. to label the stacking order. The spectra are displaced vertically for clarity. The blue and red arrows mark the SiO_2 and graphene phonons, respectively. (c) Sketch of the atomic displacements of the IR-active E_u phonon in bilayer graphene as indicated by the arrow directions.

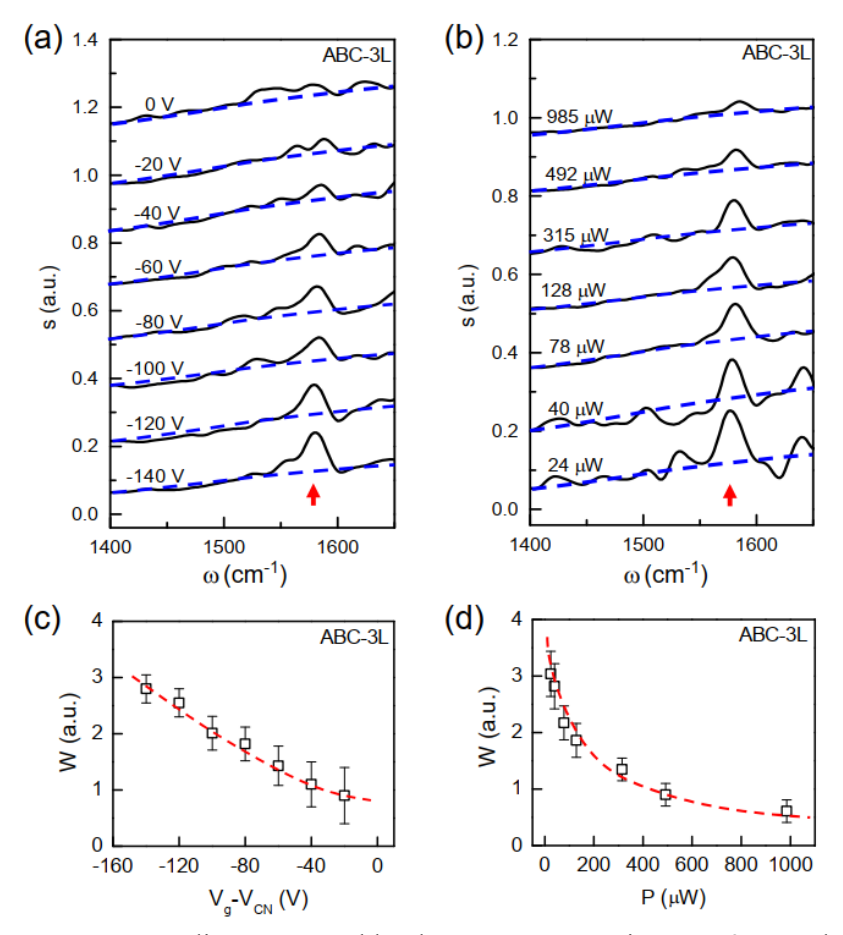


FIG. 2. (a) Nano-IR spectra revealing gate-tunable phonon resonance in ABC-3L graphene. The average power is set to be 78 μ W. The labeled voltages are V_g - V_{CN} , namely the difference between the gate voltage (V_g) and the charge neutrality point (V_{CN}) . (b) Power-dependent nano-IR spectra of ABC-3L graphene with V_g - V_{CN} = -80 V. The blue dashed curves in (a,b) mark the background signal. (c),(d) The phonon intensity W versus V_g - V_{CN} and laser power, which were extracted from (a,b), respectively. The red dashed curves here are drawn to guide the eye.

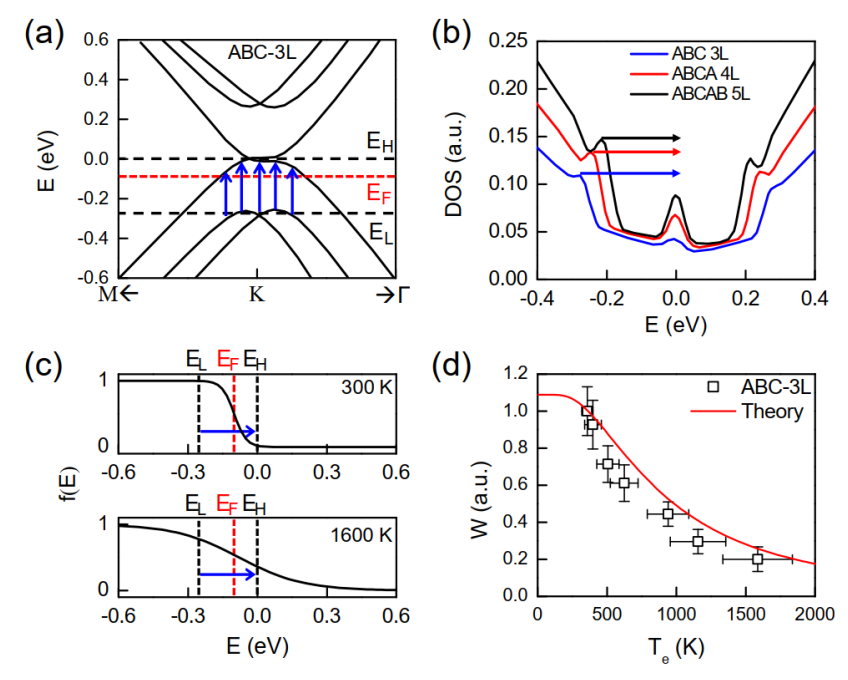


FIG. 3. (a) The band structure of ABC-3L graphene obtained with first-principle calculations [23]. The red and black dashed line marked the estimated E_F (\sim -0.08 eV) and the low (E_L) and high (E_H) energies associated with the key interband transitions (arrows). (b) The calculated DOS of various FLG samples. (c) The Fermi-Dirac distribution for $T_e = 300$ K and 1600 K, respectively. (d) Experimental and calculated phonon intensity $W(T_e)$ of ABC-3L graphene, normalized to W at P = 24 μ W and $T_e = 358$ K, respectively.

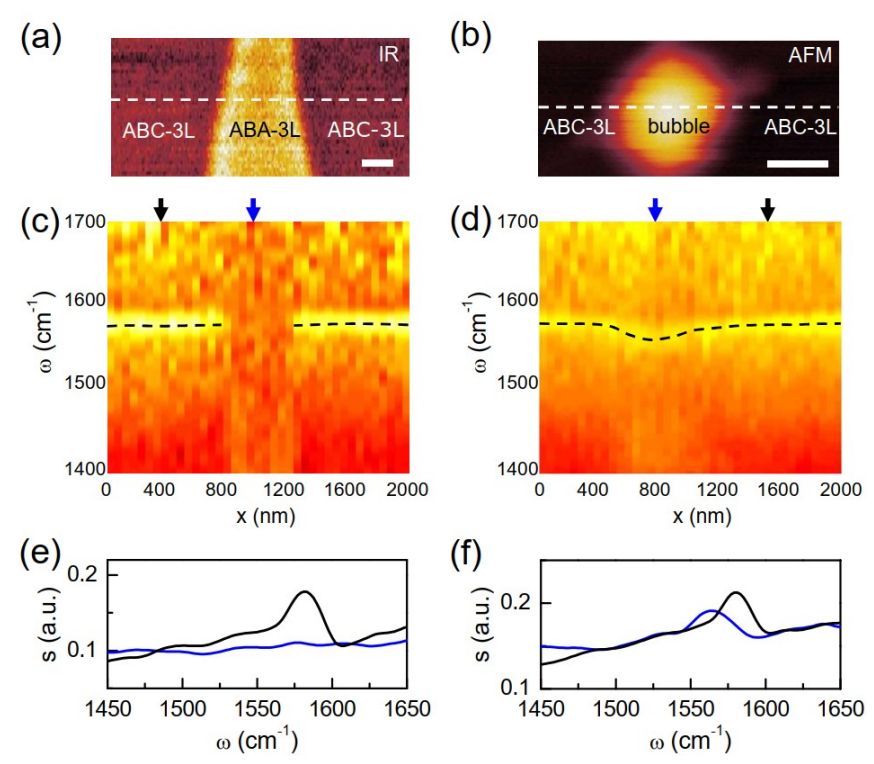


FIG. 4. (a) The nano-IR amplitude image of an ABC/ABA/ABC-3L graphene junction. (b) The AFM topography image revealing a nanobubble in ABC-3L graphene. The scales bars represent 200 nm. (c),(d) Hyperspectral maps that were taken along the white dashed lines in (a) and (b), respectively. The horizontal and vertical axes correspond to tip location (x) and IR frequency (ω) , respectively. The black dashed lines mark the peak frequency of the phonon resonance. (d) (e),(f), The nano-IR spectra extracted from the hyperspectral maps at locations marked by the arrows in (c),(d).

Supplemental Material for

Nonequilibrium phonon tuning and mapping in few-layer graphene with infrared nanoscopy

Jun Qian, ^{1,2,3} Yilong Luan, ^{1,2} Minsung Kim, ^{1,2} Kai-Ming Ho, ^{1,2} Yi Shi, ³ Cai-Zhuang Wang, ^{1,2,*}, Yun Li, ^{3,*} and Zhe Fei^{1,2,*}

J.Q. and Y.L. contributed equally to this work.

*Corresponding authors. (C.Z.W) wangcz@iastate.edu, (Y.L.) yli@nju.edu.cn, (Z.F.) zfei@iastate.edu.

List of contents

- 1. Detailed introduction about the experimental setup
- 2. Sample preparation and characterization
- 3. Additional nano-IR spectroscopy data
- 4. Phonon resonance fitting
- 5. First-principle calculations of band structures and DOS
- 6. Estimation of the electron temperatures

Figures S1 – S12

1. Detailed introduction about the experimental setup

To perform nano-infrared (IR) studies of phonons in few-layer graphene (FLG), we used a scattering-type scanning near-field optical microscope (s-SNOM, from Neaspec GmbH). The s-SNOM is built based on an atomic force microscope (AFM), so it can simultaneously obtain both topography and optical signals of the sample. For nano-IR spectroscopy measurements, the s-SNOM was excited by broadband mid-IR femtosecond (fs) pulses produced by a different frequency generator (DFG). The pulse

¹Department of Physics and Astronomy, Iowa State University, Ames, Iowa 50011, United States.

²Ames Laboratory, U. S. Department of Energy, Iowa State University, Ames, Iowa 50011, United States.

³National Laboratory of Solid-State Microstructures, School of Electronic Science and Engineering, Collaborative Innovation Center of Advanced Microstructures, Nanjing University, Nanjing 210093, People's Republic of China.

width is ~100 fs, the repetition rate is 80 MHz, and the spectral window is selected to be $1100 - 1900 \text{ cm}^{-1}$ for the studies of phonons in FLG. The average laser power (*P*) for this spectral window is tunable from 24 μ W to 985 μ W with step attenuators (www.Lasnix.com), and half of the laser power reaches the sample due to the presence of a beam splitter (Fig. S1). The pulse fluence density directly from the laser is about 0.01 J/m^2 on the sample surface, which can be significantly (2-3 orders of magnitude) enhanced by the s-SNOM tip (see Section 6 below). As illustrated in Fig. S1, the s-SNOM, the DFG system, and a HgCgTe (MCT) detector are connected in the Michelson interferometer configuration. With such a setup, we can obtain both near-field amplitude and phase spectra of the sample. In the main text, we discuss the amplitude spectra $s(\omega)$ that are ideal for revealing phonon resonances. The phase spectra are briefly discussed in Section 3 below. All the spectra are normalized to that of the gold reference. In addition to nano-IR spectroscopy, we also perform nano-IR imaging to characterize the stacking orders of FLG. For each nano-IR spectrum and image, it takes about 2 min and 20 min, respectively.

2. Sample preparation and characterization

Our FLG samples were fabricated by mechanical exfoliation of bulk graphite and then transferred onto the silicon (Si) wafers with a 300-nm-thick SiO₂ layer. Standard back gating was used to tune the carrier density of FLG. To determine the thickness and stacking orders of FLG, we used a combination of optical microscopy, AFM, and nano-IR imaging with s-SNOM. Optical microscopy is the most convenient and efficient method to determine the sample thickness. After characterizing samples with optical microscopy, we will then confirm the thickness with AFM measurements. The nano-IR imaging data simultaneously taken with AFM can be used to determine the stacking order of FLG. As an example, we show in Fig. S2 the optical microscope (OM), AFM, and nano-IR imaging data of a typical FLG sample that contains both single-layer graphene (1L) and trilayer graphene (3L). The AFM and nano-imaging data were taken simultaneously on the sample area marked in Fig. S2(a) (rectangle). With AFM and optical microscope images [Fig. S2(a,b)] as well as the AFM line profiles [Fig. S2(c)], we were able to determine the thicknesses of the sample. By performing nano-IR imaging with a continuous-wave CO₂ laser ($\omega \approx 887$ cm⁻¹) [Fig. S2(d)], we could identify two types of stacking orders within trilayer graphene. At this frequency, we are probing mainly the Drude response of FLG. The region with higher IR amplitude in Fig. 1(c) corresponds to ABA-3L graphene, which has a higher conductivity than that of ABC-3L graphene when they are equally doped. It is the same for FLG with other thicknesses. Bernal-stacked samples normally have a higher conductivity than that of rhombohedral-stacked ones. With nano-IR imaging of the Drude and plasmonic responses, we could also determine the charge-neutrality voltage (V_{CN}) of the FLG samples. All the voltages shown in the current work are difference between gate voltage (V_g) and charge neutral voltage, namely V_g - V_{CN} .

3. Additional nano-IR spectroscopy data

Gate-dependence spectra. In Fig. S3, we plot additional gate-tunable nano-IR spectra of bilayer graphene (AB-2L), ABCA-4L, and ABCAB-5L graphene. In both Fig. 2(a) and Fig. S3, we can see a clear evolution of the phonon resonance (marked with red arrows) of FLG with gate voltages. The phonon resonance is stronger at higher doping levels and is much weaker or not clearly seen close to the charge neutrality point. The physics of the doping dependence of phonons has been fully described in previous

studies [1-4]. In short, as doping (electron or hole) increases due to the increases of $|V_g - V_{CN}|$, more states are available for the key interband transitions [see Fig. 3(a) in the main text], so the interband resonance becomes stronger. According to the charged-phonon theory [5-7], the phonon resonance is strongly enhanced by interband electronic transitions due to the electron-phonon coupling. As a result, when the intensity of interband resonance increases with doping, the phonon resonance becomes stronger as well. The consistency in the responses of interband resonance and the phonon resonance upon gate tuning can be seen in the spectra of ABCAB-5L graphene [Fig. S3(c)]. Here the broad interband resonance of ABCAL-5L with a linewidth of ~500 cm⁻¹ and a peak frequency at ~1800 cm⁻¹ is partially seen in our spectral range. The peaks frequencies of the interband resonances of other FLG (e.g. AB-2L, ABC-3L, and ABCA-4L graphene) are at higher energies, thus not shown in our spectral range.

Power-dependence spectra. In Fig. S4, we plot the power-dependent nano-IR amplitude spectra of AB-2L, ABCA-4L, and ABCAB-5L graphene, where we can see the phonon resonance (marked with red arrows). The extracted intensities of phonon resonance are plotted in Fig. S5 (see Section 4 for the phonon fitting process). Like ABC-3L graphene [see Fig. 2(b,d) in the main text], the intensity of the phonon resonances decreases systematically with increasing laser power. In Fig. S4(c), we can also see that the intensity of the interband resonance of ABCAB-3L graphene (marked with a black arrow) decreases with increasing laser power. The consistency between the phonon resonance and the interband resonance upon power tuning is expected according to the charged-phonon theory. Quantitative discussions of the power dependence are given in the main text.

Nano-IR phase spectra. As discussed in the main text, the s-SNOM collects both the amplitude (s) and phase (ϕ) near-field signal. In Fig. S6, we plot gate-voltage-dependent $\phi(\omega)$ of ABC-3L graphene [Fig. S6(a)] and power-dependent $\phi(\omega)$ of ABC-3L, ABCA-4L and ABCAB-5L graphene [Fig. S6(b-d)], which were taken simultaneously with the amplitude spectra of these FLG samples [Fig. 2 in the main text and Fig. S4]. To better visualize the phonon resonance, we subtracted the spectra baseline due to interband transitions. In nearly all the phase spectra, the phonon resonance at around 1590 cm⁻¹ can be seen. Like in the amplitude spectra, the phonon peak height in the phase spectra $\Delta\phi$ also shows dependence with both gate voltage and laser power. This is expected for the weak & sharp phonon resonance sitting on the strong & broad interband resonance.

4. Phonon resonance fitting

Following previous studies [1,3], we subtracted the background or baseline of the spectra using a low-order polynomial fitting procedure. We then fit the phonon resonances in the background-subtracted nano-IR spectra with a Fano formula [1] $\Delta s(\omega) = (W/\Gamma)\{(q^2 + 2qz - 1)/[q^2(1+z^2)]\}$ with $z = 2(\omega - \omega_0)/\Gamma$, where W is the phonon intensity, ω_0 is the phonon resonance frequency, Γ is the linewidth, and q is the dimensionless parameter that describes Fano asymmetry. Here we take ABC-3L graphene as an example. The background-subtracted s-SNOM spectra and fitting spectra of ABC-3L graphene at various gate voltages and laser powers are plotted in Fig. S7. Note that the phonon resonance of the spectrum at the charge neutrality point $(V_g - V_{CN} = 0 \text{ V})$ is too weak and not identifiable.

Among the four fitting parameters, the response of the phonon intensity W is most prominent and is discussed in the main text. The other three fitting parameters ω_0 , Γ and q of ABC-3L graphene at various gate voltages and laser powers are plotted in Fig. S8 and S9 and are discussed qualitatively in the following paragraphs. To account for the responses of these parameters, we will consider two types of interband transitions here. Type-1 interband transitions are those discussed in the main text [marked with blue arrows in Fig. 3(a) in the main text and Fig. S10]. Type-2 interband transitions are from the highest-energy valence band to the lowest-energy conduction band (marked with green arrows in Fig. S10). Type-2 interband transitions in principle do not interact with E_u phonons in an ideal condition according to symmetry analysis [5]. Nevertheless, the electron-hole asymmetry and interlayer doping asymmetry might enable this "forbidden" interaction between the E_u phonon and type-2 interband transitions according to Kuzmenko et al. [1]. As discussed in Ref. [1] and the following paragraphs, type-2 interband transitions might play an important role in the responses of Γ and q due to the potential overlap between the transition energy with the phonon energy.

The phonon frequency ω_0 . As shown in Fig. S8(a) and Fig. S9(a), ω_0 decreases slightly with increasing hole doping and with increasing laser power [Fig. S9(a)]. The gate-tunable phonon softening behavior has been observed previously in far-field IR studies of both AB-2L [1] and ABC-3L graphene [4]. According to theoretical studies [5,6], the frequency shift $\Delta\omega_0$ is directly related to the phonon self-energy Π : $\Delta\omega_0 = \text{Re}(\Pi)/\hbar$. The self-energy for the zone-center optical phonons can be approximately written as:

$$\Pi \approx B \sum_{\substack{\text{interband} \\ \text{states}}} \Phi_{if} \frac{f(E_i) - f(E_f)}{\hbar \omega_0 - (E_f - E_i) + i\eta}.$$
 [S1]

Here the summation is over all available states for interband transitions, i and j label the initial and final states of interband transitions, η is a broadening parameter, B is a positive coefficient, Φ_{if} is the square of the respective electron-phonon matrix elements [5], $f(E_i)$ and $f(E_f)$ are Fermi-Dirac functions: $f(E) = \{\exp[(E-E_F)/kT_e] + 1\}^{-1}$, where k is the Boltzmann's constant. If considering only type-1 interband transitions labeled in Fig. 3(a) and Fig. S10, we have $E_f - E_i \approx E_H - E_L \approx 0.3$ eV that is larger than $\omega_0 \approx 0.2$ eV, so $\Delta \omega_0 \sim \text{Re}(\Pi)$ is negative indicating phonon softening. When increasing gate voltages, more states are available for interband transitions, so stronger phonon softening is expected. This explains the gate-tunable phonon softening behavior shown in Fig. 8(a). Equation S1 also explains the power-tunable behavior of phonon frequency shown in Fig. S9(a). As T_e increases, $|f(E_f) - f(E_i)|$ will drop systematically [see Fig. 3(c)] due to the broadening of the Fermi surface, so the phonon softening effect will be weaker at higher T_e . As a result, the phonon frequency ω_0 increases at larger laser power [Fig. S9(a)].

The phonon linewidth Γ . As shown in Fig. S8(b) and Fig. S9(b), Γ shows a weak dependence with both gate voltages and laser power. The absence of strong gate dependence of Γ in ABC-3L graphene was discovered in a previous far-field IR study [4]. We first discuss doping dependence. With increasing $|V_g - V_{CN}|$, Γ increases very slightly and then starts to decline after $|V_g - V_{CN}|$ reaches 100 V [Fig. S8(b)]. According to theory [5], Γ is directly related to the imaginary part of the phonon self-energy Π : $\Gamma = -\text{Im}(\Pi)/\hbar$. Based on Eq. S1, type-1 interband transitions tend to increase Γ , but the increase is limited due to the relatively small η (in the order of 0.01 eV) compared to $E_f - E_i - \hbar \omega_0 \approx 0.1$ eV. As suggested by

Kuzmenko et al. in their work of AB-2L graphene [1], type-2 interband transitions might play an important role in η . This is due to the potential overlap of the transition energy E_f - E_i of type-2 interband transitions with the phonon energy $\hbar\omega_0 \approx 0.2$ eV that leads to the divergence of Im(Π) (Eq. S1) and hence a sizable Γ. Note that type-2 interband transitions are only enabled when $E_f - E_i \ge 2|E_F|$, so the overlap of $E_f - E_i$ with $\hbar\omega_0$ is impossible when $|2E_F|$ is larger than 0.2 eV. Therefore, as E_F increases over 0.1 eV, which occurs as $|V_g - V_{CN}| \approx 100 \text{ V}$, the divergence of Im(Π) disappears, so one expects a drop of Γ . Indeed, we can see a slight drop of Γ in ABC-3L graphene for $|V_g - V_{CN}| > 100 \text{ V}$ [Fig. S8(b)], but the drop is much smaller compared to that observed in AB-2L graphene [1]. We argue that this is partly due to the limited gating range in our experiment ($|V_g - V_{CN}|$ is only up to 140 V, corresponding to an $|E_F|$ of 0.12-0.13 eV), and partly due to the sizable thermal broadening of Fermi level [$kT_e \sim 0.04$ eV at $P = 78 \mu W$, see Fig. S12(d)]. Now we discuss the power dependence of Γ . With increasing laser power, Γ drops slightly at low power regime (< 300 μW), and then becomes stabilized afterward [Fig. S9(b)]. Here in the power-dependence experiments, V_g - V_{CN} was set to be -80 V, corresponding to an E_F of \sim -0.08 eV, so type-2 interband transitions with E_f - E_i = 0.2 eV are enabled. These interband transitions are affected by the thermal broadening of the Fermi surface, so Γ is expected to drop with increasing laser power. Nevertheless, because $E_F \approx -0.08$ eV is very close to $E_i = -0.1$ eV, electron occupation at E_i is less than 70% at room temperature, leaving limited room for further reduction of $f(E_i)$ with increasing T_e . Also, due to the exponential dependence of $f(E_i)$ on T_e , the reduction of $f(E_i)$ occurs mainly at the low T_e region. This is consistent with our observation of a slight decrease of Γ with increasing P at the low power region [Fig. S9(b)].

The asymmetry parameter q. As shown in Fig. S8(c) and Fig. S9(c), q also varies slightly with both gating and laser power. Note that q is always negative [1,7]. For convenience, we discuss its absolute value |q| instead below. A larger |q| corresponds to a more symmetric phonon resonance. We found that |q|of ABC-3L graphene is larger than that reported about AB-2L graphene [1] indicating that ABC-3L graphene is more symmetric. This is consistent with the findings of the previous far-field IR spectroscopy [4]. We first discuss the gating responses of |q|. With increasing $|V_g - V_{CN}|$, |q| first remains constant and then slightly increases after $|V_g - V_{CN}|$ surpasses 100 V. According to the charge-phonon theory [5,6], q is directly related to the charge-phonon response function χ : $q = -\text{Re}(\chi)/\text{Im}(\chi)$. As discussed in the main text, χ can be obtained by summating $[f(E_i) - f(E_f)]/[\hbar\omega_0 - (E_f - E_i) + i\eta]$ over the relevant electronic states for interband transitions. For type-1 interband transitions, $\hbar \omega_0 - (E_f - E_i) \approx -0.1$ eV is nearly constant, so q is not sensitive to gating. In the case of type-2 interband transitions, the imaginary part of χ diverges when E_f - E_i matches the phonon energy $\hbar\omega_0 = 0.2$ eV. Therefore, type-2 interband transitions might play an important role in the responses of q [1]. Type-2 interband transition with $E_f - E_i = 0.2$ eV will be turned off when $|E_F|$ is over 0.1 eV (corresponding to $|V_g - V_{CN}| \approx 100 \text{ V}$). Therefore, we expect a drop of Im(χ) and hence an increase of |q| at higher doping, which is consistent with Fig. S8(c). The power dependence of |q|can also be understood by the effect of thermal broadening (similar to Γ , see discussions in the previous paragraph). Due to the thermal broadening, type-2 interband transitions with $E_f - E_i = 0.2$ eV are weaker at higher T_e , so |q| is expected to increase. Nevertheless, the increase is expected to be small because $E_F \approx$ -0.08 eV is very close to $E_i = -0.1$ eV [Fig. S9(c)].

5. First-principle calculations of band structures and DOS

The band structures and density of states (DOS) results shown in Fig. 3(a,b) in the main text and Fig. S11 were obtained via first-principles calculations, which were performed using density functional theory as implemented in Vienna *Ab initio* Simulation Package (VASP) [8,9]. We used Perdew-Burke-Ernzerhof exchange-correlation functional [10]. The interaction between ions and valence electrons was described by projector-augmented wave method [11]. Wavefunctions were expanded using a plane-wave basis set with the energy cut-off 400 eV. The lattice constant of graphene was set to be 2.46 Å. The atomic positions were relaxed until the forces became smaller than 0.02 eV/Å. 24×24×1 *k*-point meshes were used in the self-consistent calculations, and 360×360×1 for the calculations of the density of states. The van der Waals energy was accounted for using DFT-D3 method [12]

6. Estimation of the electron temperatures

We estimate the electron temperature (T_e) of ABC-3L graphene upon laser heating using the heat transfer module of Comsol Multiphysics. The pulse fluence density directly from the laser is about 0.01 J/m² on the sample surface (see Section 1). The pulse intensity can be strongly enhanced by the s-SNOM tip. The amount of field enhancement is dependent on the tip-sample distance (z_{tip}) that is changing due to the tip-tapping. Note that the tip-sample near-field coupling is much stronger at small tip-sample distances. Therefore, we estimate the average tip-sample distance $\langle z_{tip} \rangle$ by considering the near-field coupling weight function $q^2 \exp(-qz_{tip})$, where q is the near-field wavevector [13]. The weight function describes an exponential decay of near-field coupling with increasing tip-sample distance. The near-field wavevector q has a range of values. For approximation, we set q to be $q_0 = 1/a$ that has the strongest near-field coupling [13], where $a \approx 25 \pm 5$ nm is the radius of the tip apex. Our calculation indicates that the average tip-sample distance $\langle z_{tip} \rangle$ is about 12 nm. In Fig. S12(a), we plot the simulated in-plane field intensity ($|E_{xy}|$) map with $z_{tip} = 12$ nm. The parameters of the tip in the model were set based on our s-SNOM tip (Arrow NCPT tips from NanoAndMore). The frequency is set to be $\omega = 1500$ cm⁻¹ that is the peak frequency of our spectral range 1100 -1900 cm⁻¹. Unlike the out-of-plane field (E_z) , the strongest in-plane field $|E_{xy}|$ appears not directly underneath the tip apex, but ~40 nm away [Fig. S12(a)], where $|E_{xy}|$ is enhanced by 35 ± 5 times. The uncertainty is mainly due to the modeling parameters of the tip.

For ABC-3L graphene, σ_l is calculated to be about $1.5G_0$ on average in our spectral range when doped with a carrier density of 5.8×10^{12} cm⁻² (V_g - V_{CN} = -80 V), where G_0 = $e^2/4\hbar\approx6.08\times10^5$ Ω^{-1} is the universal optical conductivity. The corresponding optical absorption rate is about 3.4% on average in the spectral range. The electronic component of the thermal conductivity is about 100 W/m/K at our temperature range [14]. The electronic specific heat C_e is calculated using $C_e = \partial [U(T_e) - T(0)]/\partial T_e$,

where $U(T_e) = \int_{-\infty}^{\infty} Ef(E)D(E)dE$ is the energy of electrons. Our calculation indicates that C_e of trilayer graphene is roughly 2-3 times that of single-layer graphene, and it scales with T_e^2 at the high-temperature regime. We have also considered the heat transfer from hot electrons to strongly coupled optical phonons (phonons at the K and Γ points) in our heat transfer simulations following previous studies [15,16]. The simulation results are shown in Fig. S12(b-d).

Figure S12(b) plots the electron temperature (T_e , solid red) and optical phonon temperature (T_{ph} , solid black) over time right underneath the tip. In Fig. S12(c), we plot the spatial distribution of T_e at various snapshots of time. Here one can see that the highest T_e can be found ~40 nm away from the s-SNOM tip, corresponding to the location with the highest in-plane field enhancement. The electronic temperature underneath the tip is lower due to the relatively weak $|E_{xy}|$, but it is still considerably high o the thermal transport within the sample plane. Based on Fig. S12(b,c), we estimate the average T_e underneath the tip over the pulse duration. It reaches as high as ~1600 ± 250 K at full laser power and decreases monotonically with reducing laser power P. Close examination indicates that P scales roughly with T_e^3 , which is consistent with the T_e^2 scaling of electronic specific heat C_e . The uncertainty in the T_e calculations mainly comes from the estimation of field enhancement.

We have also considered the hypothetic scenario of complete thermal equilibrium of electrons and lattices upon laser excitation. In this case, the average temperature of the sample can only be increased by ~100 K above room temperature. The limited heating is mainly due to the orders of magnitude higher specific heat and thermal conductivity of the lattice than the pure electronic components. Therefore, hot electrons with average temperature up to 1600 K is indeed due to nonequilibrium heating.

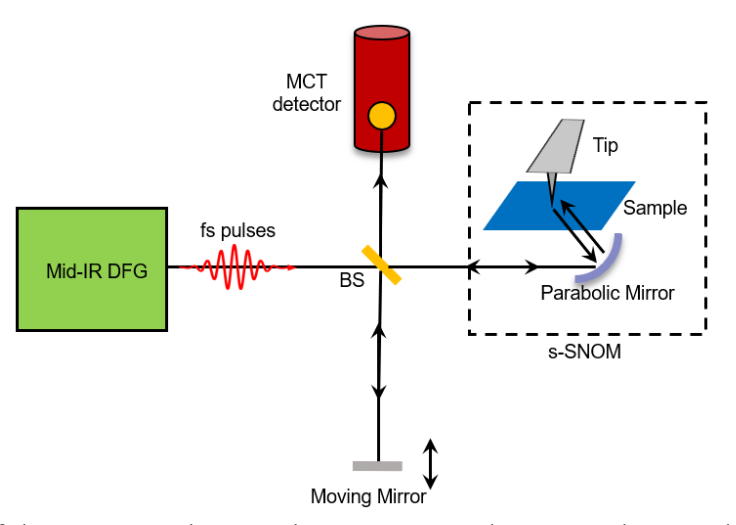


FIG S1. Illustration of the s-SNOM, the DFG laser system, and an MCT detector that are connected in a Michelson interferometer configuration.

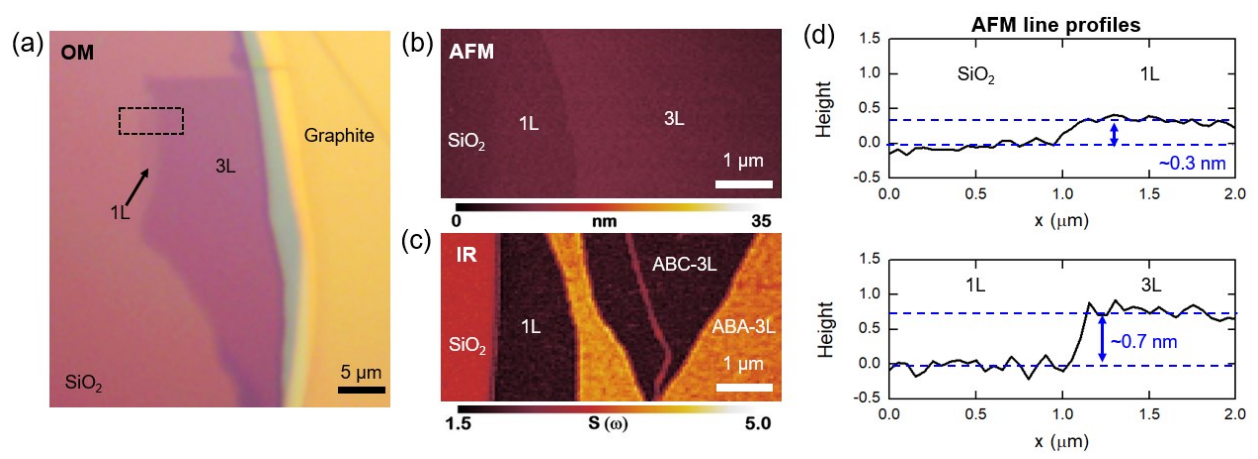


FIG. S2. (a) The optical microscopy (OM) image of the FLG sample in the main text. (b) The AFM image of the FLG sample region marked with a rectangle in (a). (c) The nano-IR image of the FLG sample region marked with a rectangle in (a) taken at 883 cm⁻¹. (d) The AFM topography profiles across the SiO₂/1L graphene boundary (top panel) and 1L/3L graphene boundary (bottom panel).

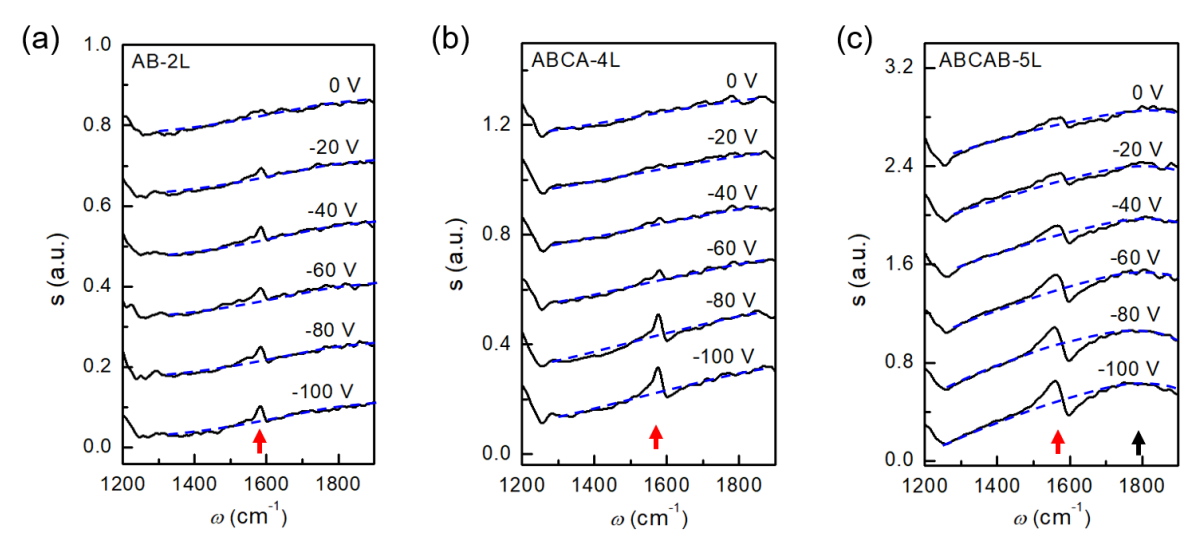


FIG. S3. The gate-tunable IR phonon resonances of AB-2L, ABCA-4L, and ABCAB-5L graphene. The average power is set to be 78 μ W, and the labeled voltages are the difference between the gate voltage and the charge-neutral voltage V_g - V_{CN} . The red arrows mark the phonon resonance of FLG. The black arrow marks the peak frequency of the broad interband resonance of ABCAB-5L graphene. The blue dashed curves mark the spectral baseline.

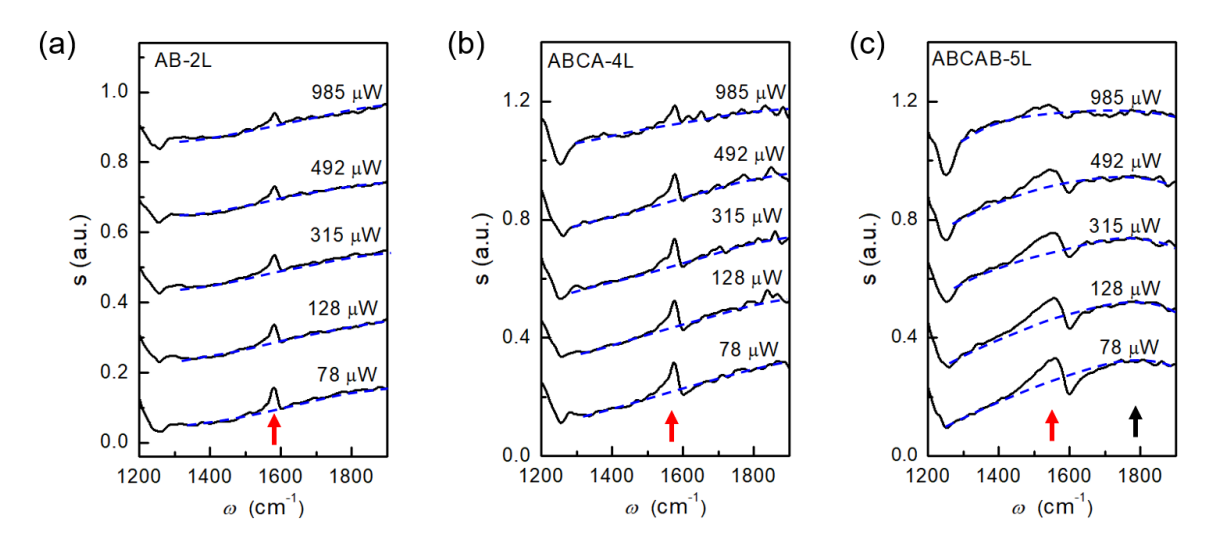


FIG. S4. Power-dependent nano-IR spectra of AB-2L, ABCA-4L, and ABCAB-5L graphene at V_g - V_{CN} = -80 V. The red arrows mark the phonon resonance. The black arrow marks the peak frequency of the interband resonance of ABCAB-5L graphene. The blue dashed curves mark the spectra baseline.

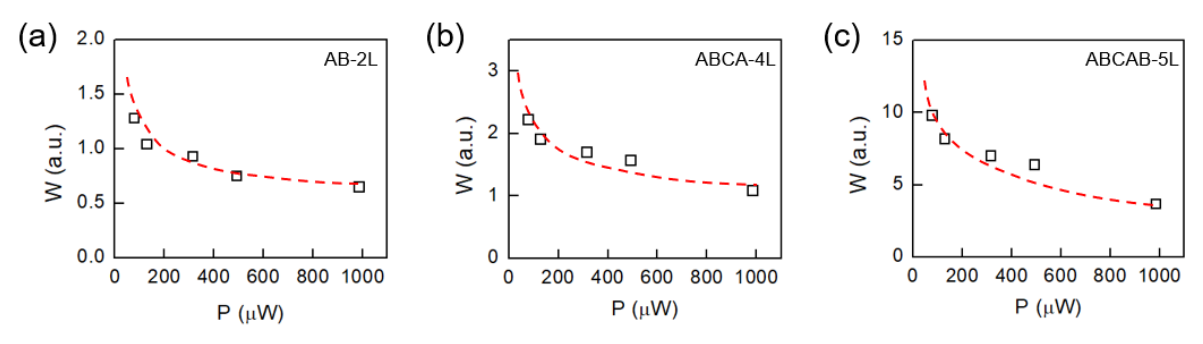


FIG. S5. The extracted phonon intensity of AB-2L, ABCA-4L, and ABCAB-5L graphene versus laser power from the spectra shown in Fig. S4. The red dashed lines are drawn to guide the eyes.

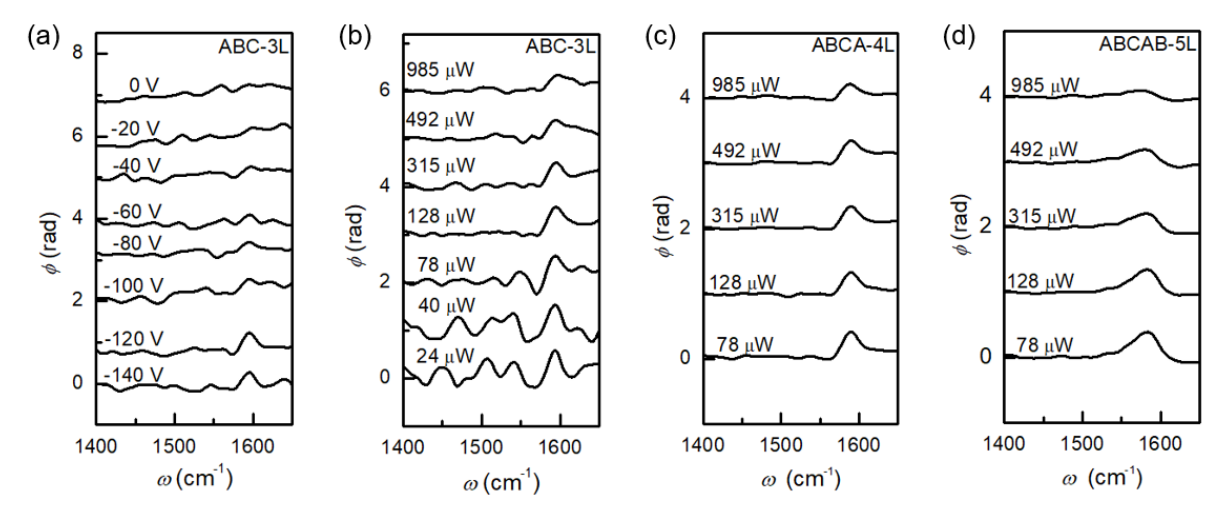


Fig. S6. (a) The nano-IR phase spectra $\phi(\omega)$ of ABC-3L at different gate voltages $(V_g - V_{CN})$. (b)-(d), The nano-IR phase spectra $\phi(\omega)$ of ABC-3L, ABCA-4L, and ABCAB-5L graphene respectively excited with different laser power.

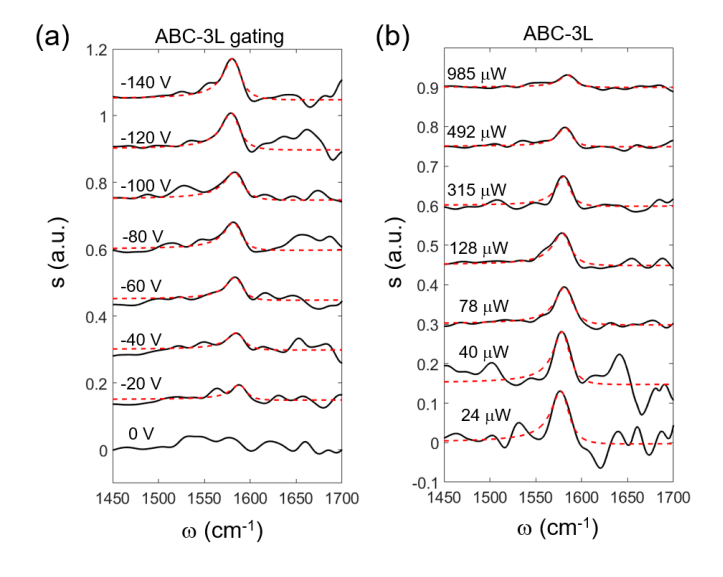


FIG. S7. Background-subtracted near-field amplitude spectra $s(\omega)$ (black) and fitting spectra (red dashed) of ABC-3L graphene with various gate voltages (a) and ABC-3L graphene taken with various laser powers (b). The phonon resonance at the charge-neutrality point ($V_g - V_{CN} = 0$ V) is not clearly resolved.

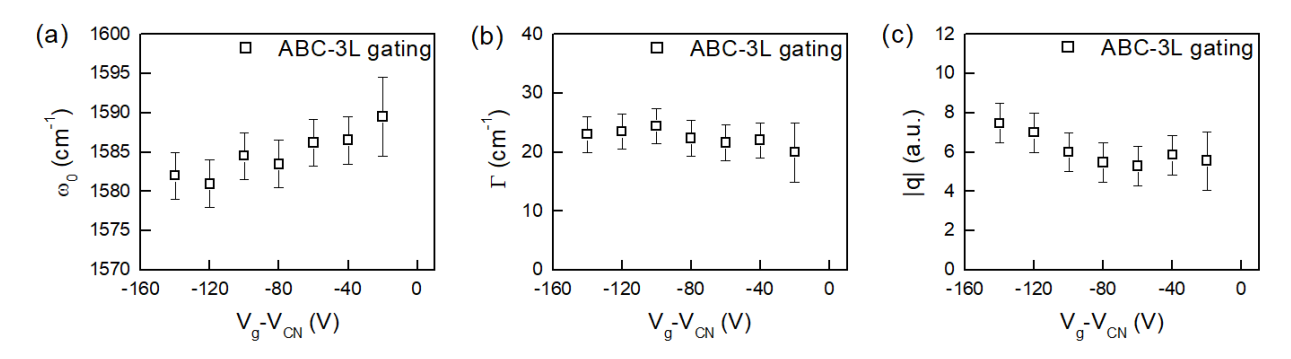


FIG. S8. The parameters ω_0 , Γ , and |q| of ABC-3L graphene at various gate voltages V_g - V_{CN} . Here laser power was set to be 78 μ W. The phonon resonance at the charge-neutrality point is not clearly resolved, so there is no data point at V_g - V_{CN} = 0 V.

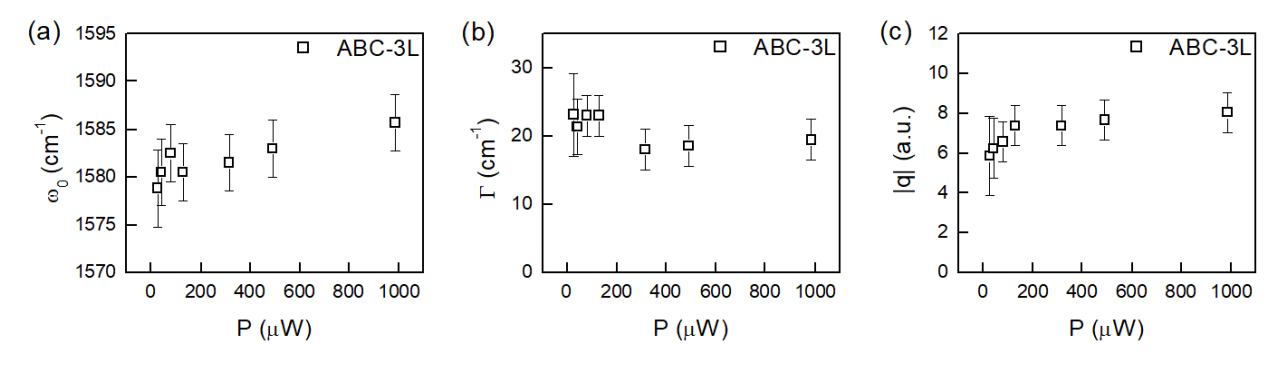


FIG. S9. The parameters ω_0 , Γ , and |q| of ABC-3L graphene at various laser powers. Here V_g - V_{CN} was set to be -80 V.

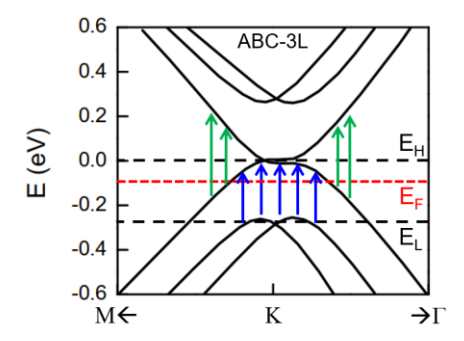


FIG. S10. Illustration of two types of interband transitions of ABC-3L graphene: type-1 (blue arrows) and type-2 (green arrows).

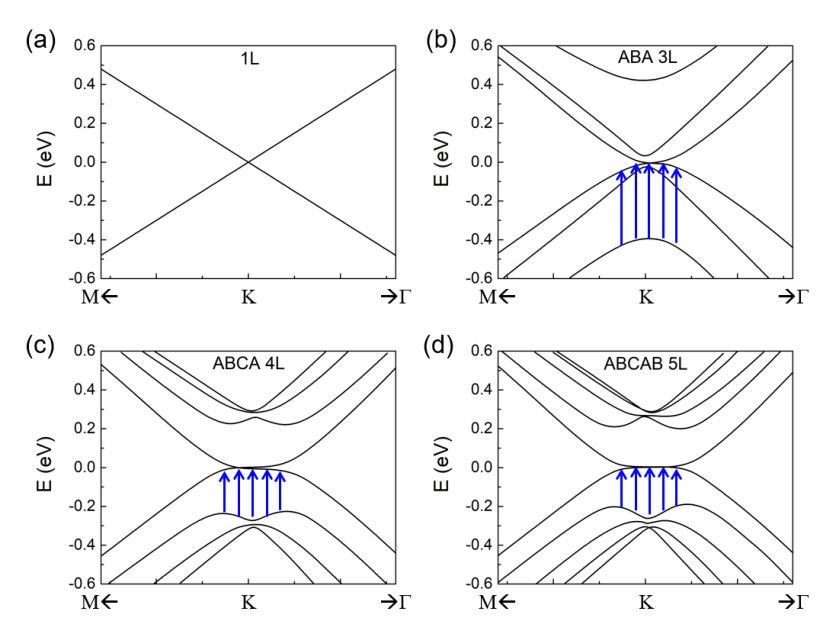


Fig. S11. The band structures of 1L (a), ABA-3L (b), ABCA-4L (c), and ABCAB-5L (d) graphene obtained from first-principle calculations. The blue arrows mark the key interband transitions responsible for the phonon intensity enhancement.

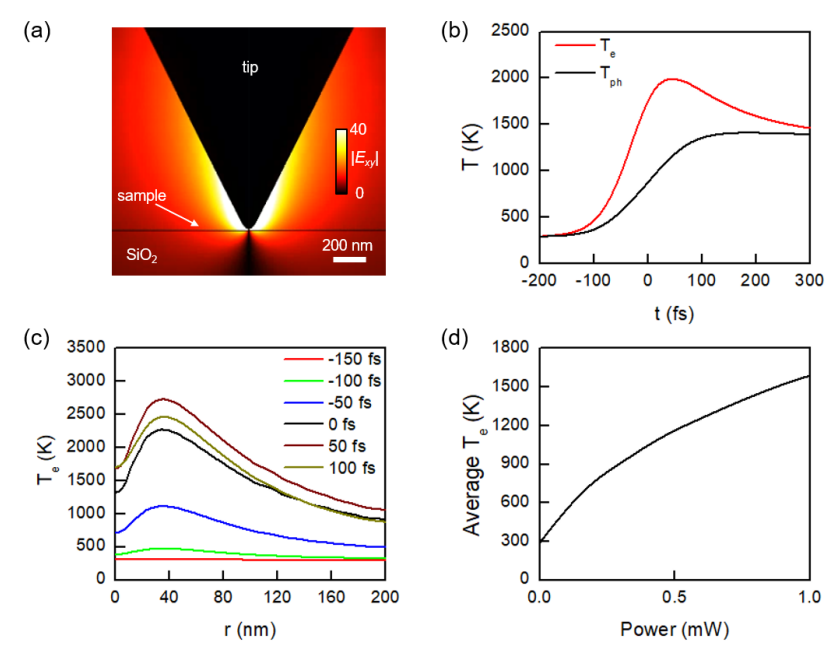


FIG. S12. (a) The simulated $|E_{xy}|$ map of ABC-3L graphene on SiO₂ under tip enhancement. (b) The calculated transient temperature of electrons (red solid) and strongly coupled optical phonons (black solid) over time underneath the s-SNOM tip (averaging for $r \le 25$ nm). At t = 0 fs, pulse intensity reaches the maximum. (c) The calculated electron temperature at various time delays versus radial distance to the tip apex (r). (d) The average electron temperature underneath the tip over the pulse duration versus excitation laser power.

References for the Supplemental Material

- [1] A. B. Kuzmenko, L. Benfatto, E. Cappelluti, I. Crassee, D. van der Marel, P. Blake, K. S. Novoselov, and A. K. Geim, Phys. Rev. Lett. **103**, 116804 (2009).
- [2] T.-T. Tang, Y. Zhang, C.-H. Park, B. Geng, C. Girit, Z. Hao, M. C. Martin, A. Zettl, M. F. Crommie, S. G. Louie, Y. R. Shen, and F. Wang, Nat. Nanotechnol. 5, 32-36 (2010).
- [3] Z. Li, C. H. Lui, E. Cappelluti, L. Benfatto, K. F. Mak, G. L. Carr, J. Shan, and T. F. Heinz, Phys. Rev. Lett. 108, 156801 (2012).
- [4] C. H. Lui, E. Cappelluti, Z. Li, and T. F. Heinz, Phys. Rev. Lett. 110, 185504 (2013).
- [5] T. Ando, J. Phys. Soc. Jap. 76, 104711 (2007).
- [6] E. Cappelluti, L. Benfatto, and A. B. Kuzmenko, Phys. Rev. B 82, 041402 (2010).
- [7] E. Cappelluti, L. Benfatto, M. Manzardo, A. B. Kuzmenko, Phys. Rev. B 86, 115439 (2012).
- [8] G. Kresse and J. Hafner, Phys. Rev. B 47, 558 (1993).
- [9] G. Kresse and J. Furthmüller, Phys. Rev. B **54**, 11169 (1996).
- [10] J. P. Perdew, K. Burke, and M. Ernzerhof, Phys. Rev. Lett. 77, 3865 (1996).
- [11] P. E. Blöchl, Phys. Rev. B **50**, 17953 (1994).
- [12] S. Grimme, J. Antony, S. Ehrlich, and H. Krieg, J. Chem. Phys. **132**, 154104 (2010).
- [13] Z. Fei, G. O. Andreev, W. Bao, L. M. Zhang, A. S. McLeod, C. Wang, M. K. Stewart, Z. Zhao, G. Dominguez, M. Thiemens *etal.*, Nano Lett. **11**, 4701 (2011).
- [14] T. Y. Kim, C.-H. Park, and N. Marzari, Nano Lett. 16, 2439-2443 (2016).
- [15] C. H. Lui, K. F. Mak, J. Shan, and T. F. Heinz, Phys. Rev. Lett. 105, 127404 (2010)
- [16] J.-A. Yang, S. Parham, D. Dessau, and Dmitry Reznik, Sci. Rep. 7, 40876 (2016).